THE JOURNAL OF PHYSICAL CHEMISTRY C
A JOURNAL OF THE AMERICAN CHEMICAL SOCIETY

pubs.acs.org/JPCC

Article

Tailoring the Transport Properties of Mesoporous Doped Cerium Oxide for Energy Applications

Federico Baiutti,*[,∇] Javier Blanco-Portals,[∇] Simone Anelli, au Torruella, Miguel Lápez-Haro, José Calvino, Sonia Estradé, Marc Torrell, Francesca Peirá, and Albert Tarancán*

Cite This: https://doi.org/10.1021/acs.jpcc.1c04861

Read Online

ACCESS | Metrics & More | Article Recommendations | Supporting Information

ABSTRACT: The hard-template nanocasted mesoporous cerium oxide possesses a unique combination of thermal stability, high surface area, and short diffusion lengths for mass and gas transport, which makes it relevant for high-temperature catalysis, sensing, and electrochemical applications. Here, we present an in-depth study of a number of mesoporous doped ceria systems, and we assess their fundamental structure and functionalities by complementary transmission electron microscopy imaging and spectroscopy, electron tomography reconstructions, and electrochemical impedance spectroscopy. We employed surface chemical modifications for increasing the ionic conductivity of the as-synthesized mesoporous Gd-doped ceria by 2 orders of magnitude, enabling the ionic pathway across mesoporous particles. Complementary bulk doping strategies (by the addition of Pr) result in the easy tuning of the electrical transport mechanisms converting pure ionic mesoporous ceria into a mixed ionic−electronic conductor. The results obtained here are rationalized in light of the local charge accumulation and mobility effects, providing a potential tool for engineering transport properties in nanocasted ceria and similar nanostructured materials for use in energy applications in the form of functional composites, infiltrated structures, or catalytic layers.

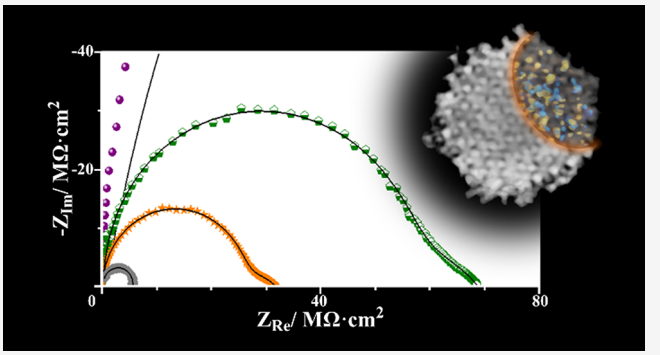

INTRODUCTION

Ordered mesoporous materials are characterized by the presence of uniform pore cavities, ranging from 2 to 50 nm, which form an open interconnected 3D network.[1,2] In such a system, each grain is potentially in contact with the atmosphere and the surface area is maximized, reaching values >1000 $m^2 \cdot g^{-1}$, while the periodicity of the arrangement ensures a homogeneous final structure.[3] Various degrees of crystallinity and different pore arrays are obtained by taking advantage of several synthesis routes, which can be applied to an extended range of functional materials including TiO_2, SnO_2, carbon, WO_{3-x}, $LiCoO_2$, and ZrO_2, just to name a few.[4−9] Mesoporous structures can therefore offer a unique combination of tailored intrinsic material functionalities, short mass- and electric-transport pathways in the solid phase, high interface density, well-defined gas transport channels, and good accessibility to the internal interfaces, which may drive fast reactivity together with rapid charge and mass transfer. Their wide applicability has been demonstrated in the last years, e.g., for catalysis,[10] solar conversion,[11] sensing,[12] separation,[13] and mass storage.[14]

Synthesis strategies are commonly based on the templating concept, in which a sacrificial replica of the final material is utilized to build the characteristic meso-sized regular pore space. Particularly, soft-template methods deal with the cooperative assembly of an organic template such as a surfactant or a co-block polymer, whereas hard-templating (nanocasting) is based on the presence of a solid preformed mesoporous template (typically carbon or SiO_2).[15] While a general drawback of mesoporous materials is the intrinsic low thermal stability, which may cause a significant decrease of the surface area and loss of mesoscale ordering,[16] silica-based templating holds great promise for the fabrication of structures capable of continuous operation at high temperatures. Almar et al. demonstrated that mesoporous doped cerium oxide fabricated from a silica KIT-6 template remains unaltered upon long-term exposure to T > 800 °C as a consequence of self-limited grain growth kinetics.[17] This opened up the possibility of applying mesoporous ceramics in the typically forbidden high-temperature energy field.[3] Particularly, nanocasted mesoporous ceria is able to take advantage of a unique combination between the ordered mesoporous structure and highly tailorable material functionalities. For example, undoped CeO_2 is a catalytically active mixed including ionic−electronic

Received: June 2, 2021
Revised: July 8, 2021

conductor that is able to accommodate abundant oxygen nonstoichiometry, and applicability in high-temperature catalysis and thermochemical fuel production is foreseen.[3,18,19] Conversely, acceptor doping (e.g., by La, Sm, or Gd) induces the formation of oxygen vacancies, making mesoporous doped ceria highly promising as electrode backbone layers in high-temperature conversion devices,[20] as also shown by recent works.[21,22] Above state-of-the-art conversion efficiencies and stable long-term performance have been reported for fuel cells and for steam and carbon dioxide electrolysis systems based on infiltrated mesoporous acceptor-doped ceria layers.[23] Scalability and compatibility with large area cell fabrication processes have also been shown.[24] Interestingly, recent studies have brought to the fore Pr-doped ceria as a potential high-temperature cathode material owing to the mixed Pr^{3+}/Pr^{4+} valence in oxidizing conditions, leading to mixed conductivity.[25]

While such results confirm the remarkable technological relevance of the material, an in-depth investigation of nanocasted ceria is missing. Local information on the mesostructured geometry and on the chemical parameters, along with a fundamental study on the electrical functionalities, would be highly beneficial for a further rational optimization of the system's electrochemical properties on the basis of the structure−function relationships.

In the present paper, starting from Gd-doped mesoporous ceria ($Ce_{0.8}Gd_{0.2}O_2$; CGO), we employ a systematic electrochemical analysis based on impedance spectroscopy (EIS) in combination with transmission electron microscopy (TEM) imaging and analysis techniques—including high-resolution TEM (HRTEM), annular dark field (ADF) and high-angle annular dark field (HAADF) imaging, energy dispersive X-ray spectroscopy (X-EDS) electron tomography (ET) reconstructions, and k-means clustering segmentation of electron energy loss spectroscopy (EELS)—to tailor the material functionalities by a twofold approach: (i) surface composition changes (by HF chemical surface etching and Co decoration) for improving the ionic conductivity (it should be noted here that such chemical post-treatments have been shown to improve the final electrochemical performance of full solid oxide cells (SOCs) based on mesoporous Gd-doped ceria according to a recent publication from our group)[23] and (ii) introduction of Pr (as a co-dopant ($Ce_{0.8}Gd_{0.2-x}Pr_xO_2$ ($x \leq 0.1$); CGPO) or as a single dopant ($Ce_{0.8}Pr_{0.2}O_2$; CPO)) for changing the transport mechanism of mesoporous ceria from purely ionic to mixed conductivity in oxidizing atmosphere. The role of dopant segregation, space-charge effects, and interparticle sintering in the final electrical properties is critically discussed. The results disclose insights into the fundamental properties of mesoporous ceria and contribute to laying the foundation for a wide implementation of such a material in the field of high-temperature energy devices.

METHODS

Powder Preparation. Mesoporous CGO, CPO, and CGPO powders were synthetized by the hard-template method with impregnation of a commercial silica template (KIT-6, ACS materials) exhibiting the characteristic *Ia3d* symmetry. $Ce(NO_3)_3{\cdot}6H_2O$, $Gd(NO_3)_3{\cdot}6H_2O$, and $Pr(NO_3)_3{\cdot}6H_2O$ precursors were dissolved in ethanol in stoichiometric proportions. After the impregnation process, the suspensions were dried at 60 °C overnight and the obtained gels were calcinated at 600 °C for 5 h. The silica template was removed through chemical etching with NaOH 2 M. An additional HF post-treatment was introduced: some of the powders were etched with HF 2.5 vol % for 1 and 5 min (the latter are indicated as HF-CGO), washed by water, and dried overnight at 60 °C. Some of the HF-CGO mesoporous powders were decorated by Co oxide to test the effect of improving the interparticle sintering. The decoration was carried out by dissolving 1 mol % of $Co(NO_3)_3{\cdot}6H_2O$ in ethanol. The mesoporous powders were put in suspension with the $Co(NO_3)_3{\cdot}6H_2O$ solution, sonicated at room temperature for 30 min, and dried at 120 °C overnight. After drying, the powders were mixed in a mortar and calcinated at 400 °C for 2 h to preserve the thermal stability of the mesostructure.

Film Preparation. The mesoporous layers for the electrochemical characterization were deposited on square films (1 cm^2) of polycrystalline alumina (Kerafol GmbH) with a thickness ≈ 30 μm. The exact thickness for each film was measured by profilometry using a confocal optical microscope. Ethanol-based inks for the deposition of the mesoporous powders via airbrushing were produced. Details about the formulation of such inks can be found elsewhere.[22] The mesoporous powders were deposited by airbrushing on top of the alumina substrates and sintered at 850 °C for 5 h (mesoporous powders without Co oxide decoration) and 800 °C (mesoporous powders with Co oxide decoration). Please note that, according to previous investigations, these temperatures ensure the structural stability of the mesoporous structure.[23] Also, please note that the expected Co oxidation state for $T < 850$ °C is 3+; i.e., Co decoration is present in the form of Co_2O_3.[26]

Electrochemical Measurements. Electrochemical impedance spectroscopy (EIS) was carried out using a Novocontrol impedance spectrometer in a frequency range of 10^6−0.1 Hz and a voltage amplitude of 0.1 V. Sputtered gold contact pads were deposited on top of the alumina substrate (separation 1 mm) to ensure the electrical connection. The measurements were carried out in a Linkam stage in the temperature range 700 to 400 °C. Please note that no cationic diffusion is expected in this temperature range. Oxygen partial pressure in the chamber was adjusted by mixing N_2 and O_2 in different proportions and measured at the outlet by a Xirox oxygen sensor.

TEM-EELS. The CPO and CGPO imaging and EELS spectrum images (SI) were acquired in a JEOL-ARM at 200 keV. The CGO and HF-CGO images were acquired in a TITAN cubed Themis, at 200 keV, equipped with an EELS Gatan Quantum ERS 966 spectrometer allowing ultra-high-energy resolution and dual-simultaneous low and core loss region acquisition. The qualitative/quantitative analysis of the EELS SI was mainly carried out in the Python-based free software Hyperspy-available (PCA denoising of the acquired spectra and background removal),[27−29] and a handful of homemade tools programmed on top of it were used to fit the multidimensional data and extract reliant data of the cation-ratio quantifications. The qualitative elemental segmentation maps were calculated using the K-means algorithm in the free scikit-learn Python library.

The cluster analysis technique employed here consists in the segmentation of the original EELS spectrum images in a user-fixed number of different regions. Each pixel is assigned to one of those possible regions according to the similarity between the EELS spectrum in that given pixel and the set of reference spectra (user-fixed number) resolved by the K-means

https://doi.org/10.1021/acs.jpcc.1c04861
J. Phys. Chem. C XXXX, XXX, XXX−XXX

clustering algorithm.[30] A clear advantage of the use of K-means is that it belongs to a family of unsupervised machine learning algorithms; thus, the segmentation does not need any user input information other than the number of clusters to resolve and the data set to analyze. Hence, the room for possible bias in the segmentation process is minimized.

TEM-ET. ET experiments on CGPO were carried out in the same TITAN cubed Themis at 80 keV, also equipped with a Chemi-STEM G2 windowless X-EDS detector. The Thermo Fisher Velox software was used to extract the mapping information for each projection. To reduce sample damage during the long acquisition times of the X-EDS ET experiment, the number of projections was kept as low as possible, starting at −70° and going to +70° each 20° (including 0°) for a total of nine X-ray maps and ADF co-acquired images to reconstruct the volume. This extremely low number of images automatically discards conventional algorithms in the reconstruction due to severe undersampling. TVM3D was the algorithm of choice,[31] a compressed sensing[32,33] algorithm based in the TVAL3 minimization routine[34,35] and implemented in MATLAB on top of the ASTRA toolbox,[36] which retrieved a highly accurate reconstruction despite the low number of experimental projections (cf. also Supplementary Figures S1 and S2).

RESULTS AND DISCUSSION

Overall Structural and Mesoporous Characterization.

In Figure 1, we report the results on the global structural characterization for the different materials under consideration. The comparison between the experimental X-ray diffraction (XRD) and the reference patterns for doped ceria is shown in Figure 1a and confirms that, for all the compositions under consideration—namely, CGO, CGPO, and CPO—phase-pure material is obtained from the synthesis (for CGPO, $x = 0.1$—10CGPO in the following—has been taken as representative). Two different surface post-treatments were explored for CGO, namely, HF exposure (2.5 vol %; HF-CGO) and Co oxide decoration (1% mol). The former was introduced to further reduce the residual silica content coming from the hard template due to the known affinity of HF to dissolve SiO_2 and to the slower etching rate with respect to Ce, Gd, and Pr oxides.[37,38] One can observe that the HF chemical post-treatment determines, after 5 min of exposure (orange line in Figure 1a; HF-CGO), the formation of secondary phases, indicated by an asterisk in Figure 1a, which are consistent with GdF_x. The expected Si content after 5 min of HF exposure is ≈0.2 wt % vs ≈1 wt % for the material as synthesized.[23] Co oxide decoration was carried out on HF-CGO with the main purpose of improving the interparticle sintering (Co-HF-CGO).[39] Also here, GdF_x-based compounds are identified as a consequence of the initial HF etching step (gray line in Figure 1a). The average lattice parameter for all the ceria-based compounds under consideration, which was calculated as an average of the d-spacing values resulting from applying Bragg's law to the different diffraction peaks, results in a lattice constant of 5.41 ± 0.01 Å. Within the resolution of the experiment, no deformation of the lattice was induced by the different dopants. Such a value is well in line with the literature on CGO and confirms the dissolution of the dopant in the bulk of the material (cf. TEM later in the text)[40] but is lower than what one would expect for Pr-containing ceria owing to the larger ionic radius of Pr^{3+} with respect to Gd^{3+}.[41] We ascribe such a finding to the presence of double valence for Pr in the as-synthesized state − Pr^{4+} presenting a lower ionic radius, as also confirmed by the mixed conductivity character of the material for $T < 600$ °C (cf. electrochemical measurements later in the text). Please refer to a previous investigation from the group (cf. ref 23) for the optimization of the surface treatments and a full structural investigation of HF-CGO and Co-HF-CGO including low-angle X-ray scattering. An initial assessment of the pore structure has been carried out by Brunauer−Emmett−Teller (BET) analysis (Figure 1b and Table 1). The results indicate that, in all cases, a mesoporous structure is present. A certain evolution of the pore size with increasing Pr content is apparent: for CGO (total BET area of 86.2 $m^2 \cdot g^{-1}$), one can observe a clear peak pore width for a pore diameter ≈ 4 nm (purple curve in Figure 1b), which is less evident in the case of 10CGPO (BET area of 63.9 $m^2 \cdot g^{-1}$, green data in Figure 1b). In the case of CPO (BET area of 56.1 $m^2 \cdot g^{-1}$, blue curve in Figure 1b), a broad distribution of pores,

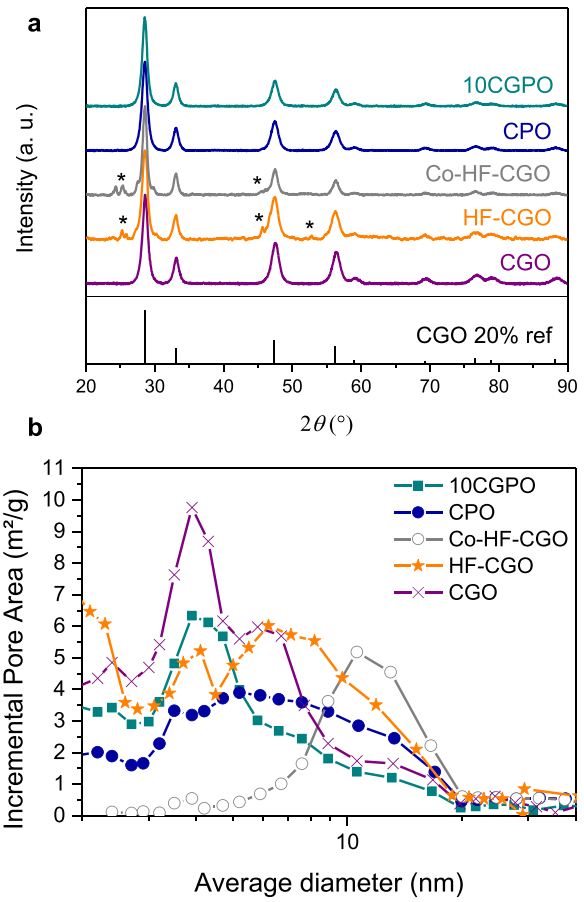

Figure 1. (a) $\theta/2\theta$ XRD patterns for mesoporous ceria. The reference CGO pattern is retrieved from JCPDS 01-075-0162. (b) BET analysis for mesoporous powders.

Table 1. BET Areas for Hard-Template Nanocasted Mesoporous Ceria

composition	BET area ($m^2 \cdot g^{-1}$)
CGO	86.2
HF-CGO	117.6
Co-HF-CGO	25.5
10CGPO	63.9
CPO	56.1

https://doi.org/10.1021/acs.jpcc.1c04861
J. Phys. Chem. C XXXX, XXX, XXX−XXX

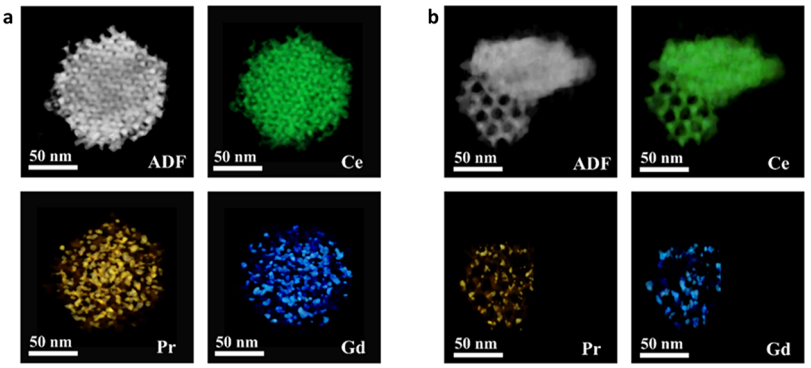

Figure 2. ET experiments of mesoporous ceria particles with nominal composition $Ce_{0.8}Gd_{0.1}Pr_{0.1}O_2$. (a) Volumes reconstructed from the ADF and elemental maps from the X-EDS signals for the packed double-gyroid structure. (b) Volumes reconstructed from the ADF and elemental maps from the X-EDS signals for the partially filled single-gyroid structure. In the elemental maps, the higher the elemental concentration is, the more saturated the color is.

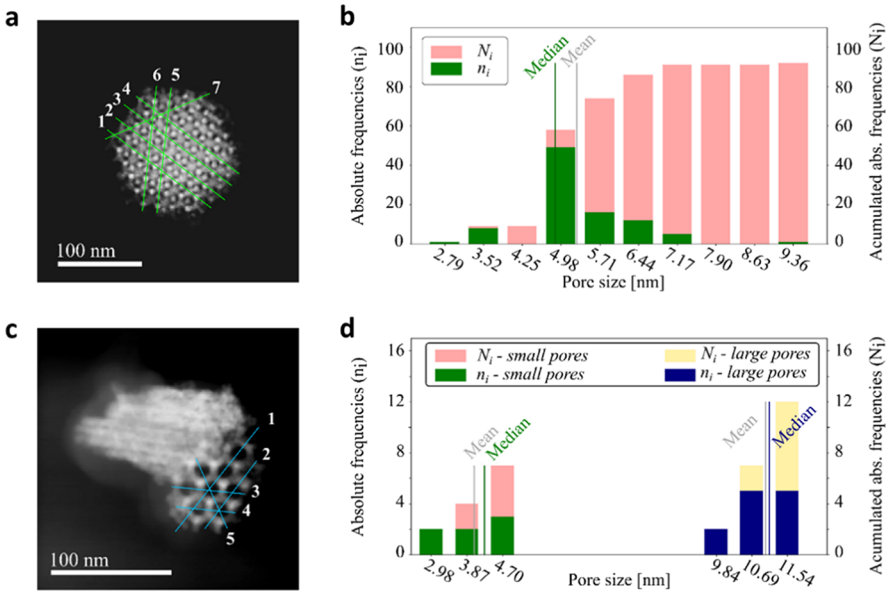

Figure 3. Study of pore distribution by electron tomography. Experimental ADF projection image (a) and histogram (b) of the pore size distribution of the packed double-gyroid structure. (c) Experimental ADF projection image and (d) histogram of the bimodal pore size distribution in the partially filled single-gyroid mesoporous structure. The lines numbered in (a) and (c), in green and blue, respectively, are the paths for the profiles used to extract the pore size distributions.

with diameters between 4 and 11 nm, is found. This suggests different fillings of the KIT-6 hard template, as discussed later in the text. A greater change in the BET area is found upon surface post-treatments of CGO. HF exposure determines an increase in the BET area up to 117 $m^2 \cdot g^{-1}$ and a certain increase of the mean pore diameter (orange curve in Figure 1b). This is consistent with surface scavenging, as discussed later in the text. Decoration by Co oxide leads to a pore area decrease (possibly due to the filling of the smaller pores), as one can clearly observe in Figure 1b (gray curve). In all cases, a high BET area > 25 $m^2 \cdot g^{-1}$, in line with previous reports, is obtained.[23]

3D Morphology of Mesoporous Particles. ET has been employed to obtain a detailed 3D reconstruction of the nanocasted mesoporous ceria particles obtained from the KIT-6 template and to retrieve global structural parameters. In Figure 2, we report ET results obtained by ADF in combination with X-EDS for the exemplary case of 10CGPO. Please note that, owing to the similar mesostructure (cf. Figure 1) and synthesis process, this analysis on 10CGPO can be qualitatively extrapolated to the other compounds as synthesized. Please refer to Supplementary Note 1 for further information on the reconstruction. The starting commercial KIT-6 template is characterized by a network of two, bicontinuous, 3D mesochannels having cubic symmetry ($Ia\bar{3}d$), which are disconnected from each other and form helical chains.[42] Such channels are impregnated by the precursors during the synthesis, and upon calcination and silica removal, a mesostructure with a long-range order is obtained. In Figure 2a, one can clearly observe the presence of the two sets of highly symmetric ceria gyroidal nanowires that result from the perfect replica of the KIT-6 with filling of both helix mesochannels (double gyroid). Such ceria nanowires are expected to be connected by pillars and leave a free volume network with a pore size of a few nanometers.[43] In Figure 2b, the volume rendering of another particle, obtained by the same synthesis route, is shown: Here, the structure is characterized by a much more open pore structure that stems from the filling of only one of the channels of the KIT-6 template (single gyroid). This particle also exhibits a nonordered region coming

https://doi.org/10.1021/acs.jpcc.1c04861
J. Phys. Chem. C XXXX, XXX, XXX−XXX

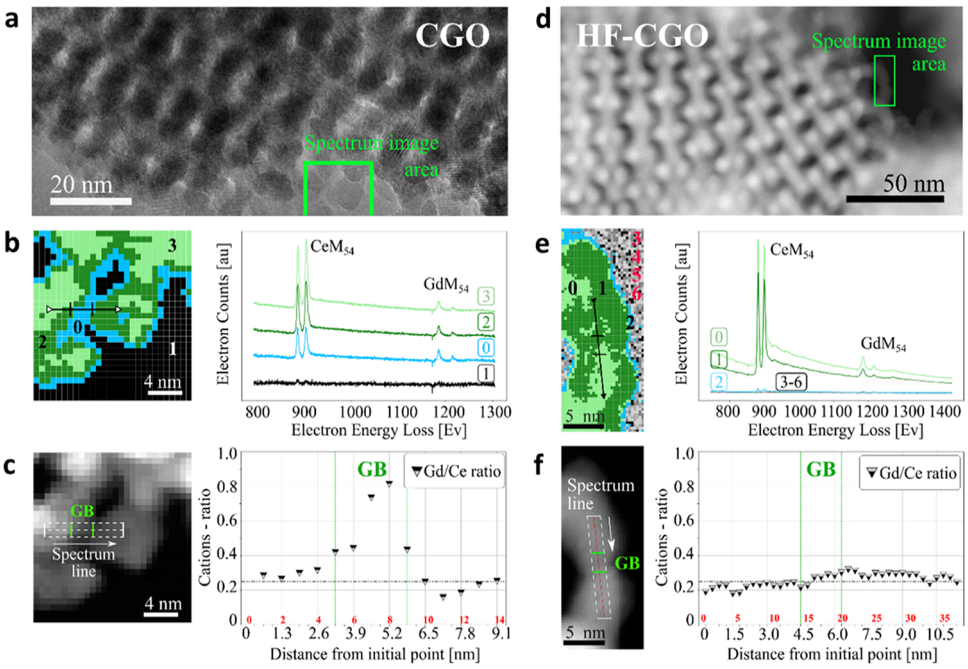

Figure 4. Conventional 2D TEM imaging and spectroscopy for the as-synthesized CGO and HF-CGO. HRTEM image of the as-synthesized CGO (a) and HAADF image for the HF-CGO (d) structure. The areas where the EELS spectrum images were acquired are marked in green in (a) and (d). The segmented color maps of the spectrum image areas and their corresponding reference spectra resolved by the K-means algorithm are shown in (b) for the as-synthesized CGO and in (e) for the HF-treated CGO. The co-acquired ADF images, with the paths for the line-scan analysis overlaid on top, and the cation ratio quantified from the EELS signals along those lines are shown in (c) for the as-synthesized CGO and (f) for the HF-treated CGO. The grain boundaries crossed by the line-scans are marked in both the ADF images and the scatter plots for the cation-ratio quantification. The numbers in red inside the scatter plots are the pixel positions along the line-paths corresponding to the distances (nm) in the *x* axis.

from incomplete template filling. The simultaneous appearance of different structures (single gyroid, double gyroids, and irregular) is typical of hard-template nanocasting methods and is also consistent with previous global microstructural investigations from our group including small-angle X-ray scattering.[23,44] Please note that single- or double-gyroid KIT-6 templates can be obtained by appropriately tuning the hydrothermal treatment of the reactants during the synthesis.[45]

The ADF volume reconstructions and X-EDS projection maps of the constituting cations (Ce, Pr, and Gd), which are shown in the corresponding panels of Figures 2a,b (for the double and single ceria gyroid, respectively), provide a spatial mapping of their distribution. Particularly, while the structure skeleton is characterized by a homogeneous distribution of Ce, the dopants (Pr and Gd in this exemplary case) distribute less evenly, revealing a clear tendency of such elements to segregate toward the junctions of the mesostructure nodes. In any case, the comparison of elemental maps reveals that even in these high-dopant-concentration sites, all three lanthanides remain mixed at the atomic level.

Dopant segregation in complex oxides is thermodynamically driven (as a consequence of strain effects and/or electrostatic forces) and becomes kinetically active during the synthesis of the material, as widely reported:[46−48] For example, in the case of $Ce_{0.8}Gd_{0.2}O_2$ fabricated by the chemical route, Lei et al. have reported Gd/Ce up to 0.7 at the grain boundaries,[49] whereas Bowman et al. observed a Gd site occupancy fraction ranging from 0.4 to 0.7 with a dopant segregation width of approximately 1.8 ± 0.3 nm,[50] consistent with this work. A quantitative analysis by conventional 2D TEM is presented later in the text. In Figure 3, we provide statistical analysis giving quantitative information on the pore size distribution. In the case of the double gyroid (Figure 3a, ADF projected image), the packed structure leaves a monomodal pore distribution with an average pore size ≈ 5 nm (Figure 3b). The much more open porosity of the single-gyroidal structure (Figure 3c, ADF) leads instead to a bimodal pore distribution (Figure 3d). The majority of the pores has a size ≈ 10 nm, yet a minority fraction of smaller pores, deriving from a partial filling of the template, is present. The presence of single and double gyroids in the final ceria mesostructured determines the final bimodal pore distribution highlighted by BET for the as-synthesized materials (cf. Figure 1b). Further details of the pore measurement process from the ADF images are detailed in the Supplementary Note 2 and Supplementary Figures S3 and S4. Resolving the grain size distribution from these intricate 3D materials is a challenging task. As extensively described in Supplementary Note 3, direct observation places the sizes in a range between 3 and 7 nm, with occasional larger structures that could be ascribed to ensembles of grains sharing the same axis. Overall, the grains appear to be randomly oriented and neighbor grains do not necessarily share the same orientation (i.e., different zone axes are resolved for contacted grains).

Improving the CGO Ionic Conductivity by Surface Chemical Modification. 2D HRTEM imaging and spectroscopy on as-synthesized mesoporous CGO are shown in Figure 4a. Such an analysis has been performed to obtain a quantitative analysis of the local dopant distribution. In the HRTEM image (Figure 4a), one can observe a long-range order at the mesoscale. We analyzed a specific area (highlighted by the green rectangle in panel a) for in-depth

https://doi.org/10.1021/acs.jpcc.1c04861
J. Phys. Chem. C XXXX, XXX, XXX−XXX

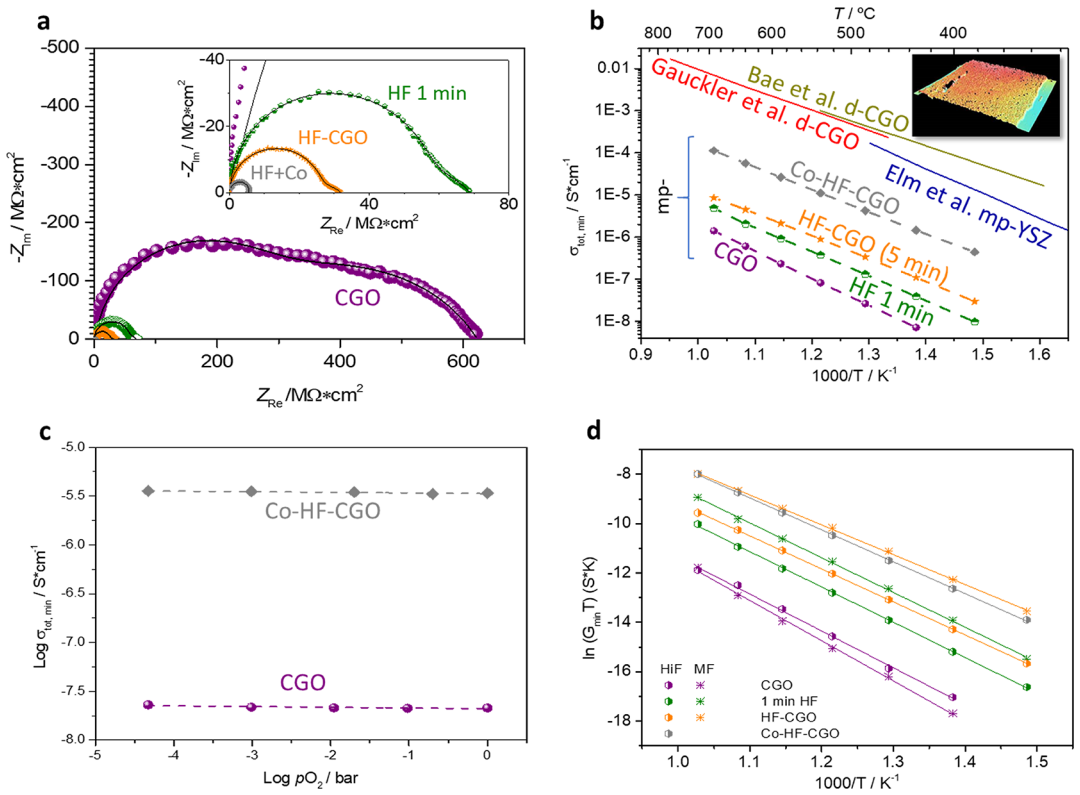

Figure 5. Electrochemical properties of mesoporous CGO films. (a) Nyquist plots at 650 °C in dry air for CGO as synthesized (purple symbols), after HF exposure (green and orange symbols for 1 and 5 min exposure, respectively), and after Co decoration of 5 min HF-etched powders (gray simbols). The black line represents the results of the fitting, performed using a series of two R//CPE elements. (b) Total conductivity as a function of inverse temperature. Here, d = dense and mp = mesoporous. Gauckler et al. (dense films with an average grain size ≈ 75 nm) after ref 54; Bae et al. (dense films with an average grain size of 50 nm) after ref 55; and Elm et al. (mesoporous YSZ filmss) after ref 9. (c) Oxygen partial pressure dependence for the total conductivity in CGO as synthesized (purple) and Co-HF-CGO (gray). (d) Arrhenius plots for the single-impedance contributions in terms of conductance G (HiF: closed symbols and MF: open symbols).

chemical analysis via EELS cluster analysis (panel b) and EELS spectrum line-scans (panel c). The cluster analysis provides an extended spatial mapping for the dopant distribution along the grains. A difference in the energy spectra of the surface and bulk cluster signals can be observed in terms of the intensity ratio between the Gd white lines (WLs; sharp features on the spectra at 1185−1217 eV of energy loss) and the Ce WLs (883 and 901 eV). Particularly, the relative intensity of the Gd WLs is higher in the grain boundary regions (areas 0 and 2 in panel c) with respect to the bulk (area 3). In the EELS line-scan of CGO (Figure 4e), the quantification of the spectra by the Egerton method[51] reveals that the Gd/Ce molar ratio increases up to ≈0.8 at the grain boundaries for the as-synthesized material. The width of the Gd-rich areas is about 4 nm. Owing to the very narrow segregation region, the Gd/Ce ratio in the bulk stays basically unaffected and is consistent with the nominal value (Gd/Ce ≈ 0.25). This highlights in greater detail the extent of the elemental segregation of Gd toward grain free surfaces and grain boundaries (GBs), in agreement with the global particle reconstruction presented earlier in Figure 2.

In a previous publication from our group,[23] we showed that the introduction of an HF postprocess to the synthesis of mesoporous CGO (5 min exposure to 2.5 vol % HF) can be implemented for the fabrication of high-performance SOCs based on a mesoporous scaffold. There, we showed that HF exposure contributes to removing residual SiO_2 from the KIT-6 template. In the present work, we analyze the effect of HF etching in terms of surface composition and in particular of dopant segregation. In Figure 4d (low-magnification HAADF of HF-CGO), one can observe that the typical long-range order of the structure is maintained, demonstrating no apparent major structural degradation upon HF exposure (please note that, according to BET—cf. Figure 1—HF treatment determines an increase of the pore width). More importantly, the cluster analysis (Figure 4e) highlights no apparent difference between the spectra corresponding to the bulk and those of the GB clusters, which indicates that a much more homogeneous Gd distribution is present. The EELS line-scan of HF-CGO (Figure 4f) clearly shows that no Gd segregation is present; i.e., the HF etching post-treatment promotes scavenging of the Gd-rich regions. This is in agreement with the XRD analysis shown in Figure 1, in which the formation of GdF_x secondary phase precipitates upon HF etching was pointed out.[23] This is also in agreement with the BET analysis highlighting an increase of the average pore width upon HF etching (cf. Figure 1): HF determines the scavenging of the pore walls, where Gd is segregated, which results not just in the removal of the Gd segregation areas but also in a net increase of the pore diameter.

EIS was carried out to investigate the fundamental transport properties of the as-synthesized CGO under controlled conditions of temperature and synthetic atmospheres. The results are summarized in Figure 5. Here, we also examine the impact of surface compositional changes on the electrical conductivity of mesoporous CGO as a result of HF exposure

https://doi.org/10.1021/acs.jpcc.1c04861
J. Phys. Chem. C XXXX, XXX, XXX−XXX

(1 and 5 min) and of Co oxide decoration. (Please note that Co oxide decoration is carried out at reduced temperatures—cf. also the experimental section—to prevent Co diffusion in the grain interior and that, owing to the small concentration (1 mol %), no direct observation of Co distribution was possible by TEM techniques owing to detection limits.) All the electrical measurements in the present work have been carried out in an in-plane configuration on films obtained by airbrushing on an alumina support (see the experimental section for more details). Although this fabrication process determines a high residual porosity (≈50% measured by Archimedes's method), airbrushed layers are of high technological relevance, so direct information on the properties of functional layers can be retrieved by the measurements.[24] In the following, we will refer to $\sigma_{tot,\ min}$ as the conductivity retrieved from the measured total impedance and considering only the macroscopic sample geometry; i.e., $\sigma_{tot,\ min}$ is an averaged value considering both the solid phase and pore network and therefore represents a bottom value for the intrinsic material's conductivity. A similar approach has been followed, e.g., by Hartmann et al., for the study of mesoporous thin films based on CeO_2-ZrO_2 solid solutions.[52] It should be noted here that such a configuration induces the presence of a parallel $(RC)_{stray}$ circuit induced by the polycrystalline alumina substrate. While the measured substrate resistance is at least 1 order of magnitude higher than the most resistive films under consideration and can therefore be neglected, we estimate the parallel stray capacitance C_{stray} to be about 1 order of magnitude higher than the bulk capacitance of our ceria films ($C_{stray} \approx 1.2{\cdot}10^{-13}$ F vs $C_{bulk} \approx 1{-}3{\cdot}10^{-14}$ F depending on the film thickness). As a consequence, phenomena characterized by $C \leq C_{stray}$ are expected to appear in the impedance plot as a single semicircle having a resistance equal to the sum of the contributions and capacitance C_{stray}. In Figure 5a, representative impedance spectra obtained at $T = 650$ °C in air atmosphere are shown. Two main impedance contributions can be clearly separated (material as synthesized, after 1 and 5 min etching; cf. also capacitance values in Supplementary Table S1), whereas the film based on Co-HF-CGO is dominated by one contribution. Please note that according to the analysis of the distribution of relaxation times (DRT; Supplementary Figure S9), additional minor low-frequency contributions (characteristic frequency < 10 Hz) may appear. These are ascribed to the film/electrode interface and are not further considered in the analysis.[9] The film impedance response has been modeled as a series of two ZARC elements ($R_{HiF(MF)}//Q_{HiF(MF)}$, Q constant phase element), which are typically employed for the analysis of electrical conduction mechanisms.[53] The derived true capacitance values C for the high-frequency (HiF) and for the-medium frequency contributions (MF) are in the order of $C_{HiF} = 2{-}5{\cdot}10^{-13}$ F ($1{-}4{\cdot}10^{-11}$ F/cm; please note that this value is very similar to C_{stray}) and between $5{\cdot}10^{-11}$ and $1{\cdot}10^{-10}$ F for C_{MF} ($4{-}9{\cdot}10^{-9}$ F/cm). Interpretation of the impedance arcs will be given later in the text. First, an analysis based on the total film impedance ($R_{HiF} + R_{MF}$) is provided.

For a longer exposure time of CGO to the HF solution (up to 5 min), we observe a clear decrease of the total impedance (Figure 5a). An additional improvement is also obtained by Co decoration. In Figure 5b, the total conductivity values ($\sigma_{tot,\ min}$) are reported as a function of inverse temperature, alongside a 3D confocal microscopy view of the mesoporous thin-film layer (inset). Here, as a useful comparison, we also report literature values for nanocrystalline dense CGO films and for mesoporous films of a related electrolyte material, namely, yttria-stabilized zirconia (YSZ).[9,54,55] Please note however that a comparison on the intrinsic conductivity values is here hindered by the high porosity of the films (≈50%). As highlighted by Pérez-Coll et al.,[56] at such high levels of porosity, the grain-boundary transport is modified (i.e., the effective path is poorly defined, and the ionic conduction is hindered by weak particle-to-particle bonding), so no information on the specific transport properties is directly accessible. The reported literature values for dense structures should therefore only be taken as the upper theoretical limit for the conductivity. In the following, our analysis will only deal with relative comparisons between similar structures having different compositions. One can observe that HF-CGO (5 min exposure) exhibits ≈10 times larger conductivity than as-synthesized CGO at 720 °C ($2.2{\cdot}10^{-6}$ vs $3.5{\cdot}10^{-7}$ S·cm^{-1}). Co decoration of the HF-CGO powders yields an increase of $\sigma_{tot,\ min}$ for an additional order of magnitude (Co-HF-CGO, $\sigma_{tot,\ min} = 2.8{\cdot}10^{-5}$ S·cm^{-1} at 720 °C). Interestingly, despite the large improvements obtained by the post-treatments, the final conductivity values that we obtained are still more than 1 order of magnitude than mesoporous YSZ films obtained by evaporation-induced self-assembly (dark blue line in Figure 5b).[9] This suggests a strong influence of the synthesis route in the final functionalities. It should be noted however that self-assembled structures are typically characterized by a poorer thermal stability and are typically not suited for high-temperature application (unlike nanocasted ceria).[17,52] In Figure 5c, the oxygen partial pressure dependence pO_2 for the total conductivity is shown: The flat horizontal lines ($m = \pm 0.02$ for all the illustrated cases) indicate the main ionic character of the material at least down to $pO_2 \approx 10^{-5}$ bar.[20] Please refer to Supplementary Figure S10 for the pO_2 dependence of the single-impedance arcs (HiF and MF), also showing a flat behavior.[57] Here, only representative samples (namely, CGO as synthesized and Co-HF-CGO) are shown. This allows also the exclusion of a large contribution of a surface electrical transport pathway, which is expected to be influenced by the local gas/solid equilibrium.[58]

Notwithstanding the complexity of the system, specific information on the effect of the chemical post-treatments can be discussed by considering the trends of the impedance contributions upon HF exposure and Co decoration. The Arrhenius plot for the MF and HiF arcs is depicted in Figure 5d, and the respective activation energies are reported in Table 2.

It can be observed that the post-treatments have a beneficial effect both on the HiF and in the MF arcs not just in the absolute values but also in decreasing the activation energy of the related transport processes. It also becomes apparent that the MF contribution is more decisively affected and is no

Table 2. Activation Energy for the Different Impedance Contributions in Mesoporous CGO Films

	as-synth. CGO	1 min HF	5 min HF (HF-CGO)	Co-HF-CGO
HiF (eV)	1.28 ± 0.01	1.23 ± 0.01	1.15 ± 0.01	1.11 ± 0.01
MF (eV)	1.40 ± 0.01	1.21 ± 0.01	1.04 ± 0.01	
total conductivity	1.35 ± 0.01	1.23 ± 0.01	1.14 ± 0.01	

https://doi.org/10.1021/acs.jpcc.1c04861
J. Phys. Chem. C XXXX, XXX, XXX−XXX

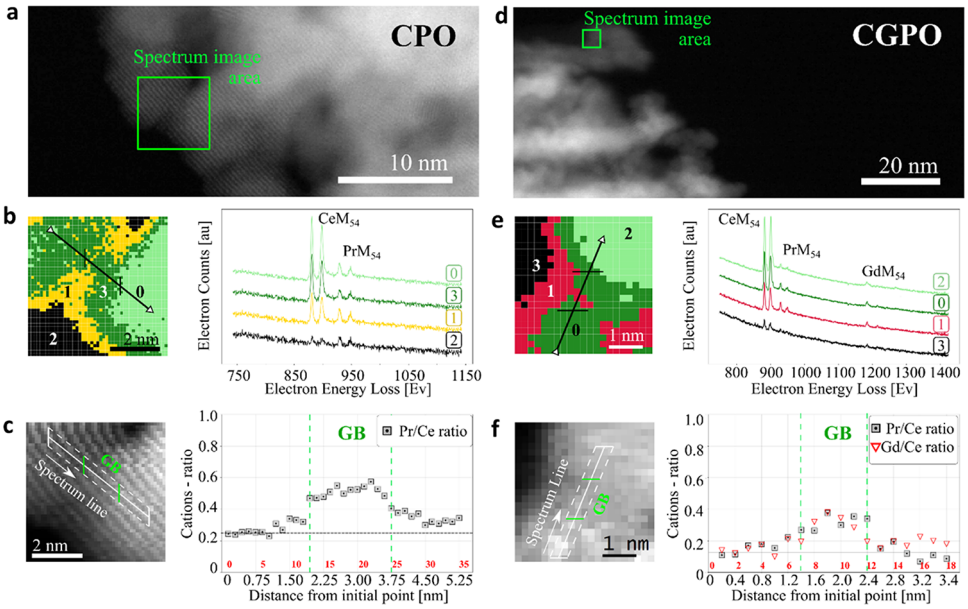

Figure 6. HAADF images of the mesoporous structures for (a) CPO and (b) CGPO. The areas where the EELS spectrum images were acquired are marked in green in (a) and (b). The segmented color maps of the spectrum image areas and their corresponding reference spectra are shown in (c) for the CPO and in (d) for the CGPO. The co-acquired ADF images, with the paths for the line-scan analysis overlaid on top, and the cation ratio quantified from the EELS signals along those lines are shown in (e) for the CPO and (f) for the CGPO. The grain boundaries traversed by the line-scans are marked with a GB in green in both the path markings overlaying the ADF images and the scatter plots for the cation-ratio quantification. The numbers in red inside the scatter plots are the pixel positions along the line-paths corresponding to the distances (nm) in the *x* axis.

longer limiting the conductivity for the case of the Co-decorated sample. According to the TEM investigations and to previous analysis from our group,[23] the chemical post-treatment by HF has a twofold effect: removal of Si impurities and scavenging of the grain surfaces where the dopant is segregated. It is now possible to directly correlate this with the measured electrochemical properties. Particularly, it is interesting to notice that Si removal is not expected to determine a change activation energy for the ionic conduction. As reported previously,[59] the blocking effect of insulating silica leads to current striction. As a consequence, its removal determines the occurrence of new current pathways that directly translate into an increase of conductivity yet with no change in the conduction mechanism.[60] In our case, the observed improvement of conductivity in HF-CGO is therefore only partially ascribable to Si removal. To explain the decisive reduction in the activation energy (from 1.35 ± 0.01 eV (as-synthesized CGO) to 1.14 ± 0.01 eV (5 min HF-exposed CGO) for the total conductivity), one should refer to the removal of the Gd-segregation area on the ceria GBs (cf. Figure 4). Such highly doped regions are expected to act as a strong barrier to oxygen migration owing to scattering. Their removal by HF etching corresponds to an enhancement of the oxygen mobility, i.e., a decrease in the activation energy (arguably, of both migration enthalpy and the temperature-independent prefactor),[61] in agreement with our experimental data. It should be mentioned, however, that not only mobility effects are to be considered for ceria GBs, as concentration effects are expected and in particular oxygen vacancy depletion as a consequence of space charge.[62,63] For the doping level under consideration, the expected GB conductivity is about 2 orders of magnitude lower than the bulk,[59,64] and the GB thickness is ≈2−4 nm.[65] In our case, owing to the nanocrystalline nature, this becomes comparable to the grain size (<10 nm, cf. TEM). The expected depletion of the total ionic conductivity, in agreement with a previous report on nanocrystalline heavily acceptor-doped ceria, is about 1 order of magnitude.[57] Also consistent with literature, blocking-boundary effects deriving from space charge can be considered responsible for the final activation energy (1.14 ± 0.01 eV for HF-CGO after 5 min exposure) being higher than the expected bulk value (≈0.7 eV).[66] Interestingly, while a net positive effect on oxygen mobility derives from removing the Gd excess at the GBs, the accumulation of such negatively charged species in the as-synthesized material partially screens the positive space-charge potential. The removal of Gd excess at the GBs by HF etching is therefore expected to lead to further oxygen vacancy depletion in the space-charge region.

As far as the effect of Co decoration is concerned, one should consider that the addition of Co on the powder surface is expected to act both as a sintering aid[39] and as an effective dopant, i.e., to improve the intrinsic grain boundary conductivity by reducing the space-charge potential.[67,68]

Our investigation did not highlight a direct effect on the conduction mechanism, as demonstrated by the unchanged activation energy of the Co-decorated HF-CGO with respect to the 5 min HF-treated sample. We conclude that Co mainly acts as a sintering aid, enhancing the lateral contact area between the grains and opening up additional paths for current flow.

As anticipated previously, the identification of the conduction processes based on the associated time constant is not unambiguous owing to C_{stray}. To the lowest measured capacitance $C_{HiF} = 2-5\cdot10^{-13}$ corresponds a relative dielectric constant $\varepsilon_{\rho,HiF} \approx 980-1290$ (again considering a porosity of 50%), which is compatible with previous reports on ceria grain boundaries.[65] Therefore, one can assume the high-frequency arc to derive from the convolution of bulk and grain boundary

https://doi.org/10.1021/acs.jpcc.1c04861
J. Phys. Chem. C XXXX, XXX, XXX−XXX

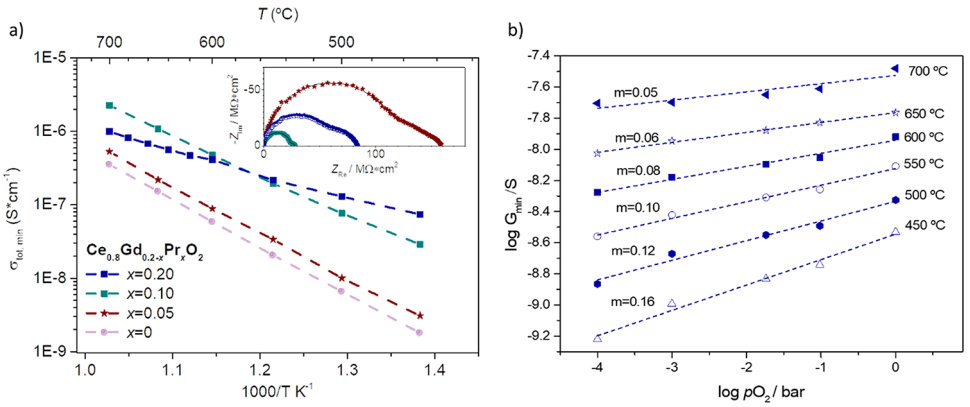

Figure 7. Electrochemical properties of $Ce_{0.8}Gd_{0.2-x}Pr_xO_2$ mesoporous films. (a) Minimum total conductivity as a function of inverse temperature for x = 0 (purple), x = 0.05 (red), x = 0.10 (green), and x = 0.20 (blue). In the inset, Nyquist plots at 650 °C in oxygen atmosphere. Here, the black line is the result of the fitting to the experimental data using a series of two ZARC elements. (b) pO_2 dependence for $Ce_{0.8}Pr_{0.2}O_2$ in the temperature range from 450 to 700 °C.

Table 3. Activation Energy for the Electrical Conductivity for $Ce_{0.8}Gd_{0.2-x}Pr_xO_2$, x = 0 (CGO), 0.05 (CGPO15-5), 0.1 (10CGPO), and 0.2 (CPO)[a]

	CGO	CGPO15-5	CGPO10-10	CPO (T > 600 °C)	CPO (T < 600 °C)
HiF (eV)	1.28 ± 0.03	1.28 ± 0.01	1.11 ± 0.02	1.07 ± 0.02	0.77 ± 0.06
MF (eV)	1.40 ± 0.01	1.45 ± 0.05	1.23 ± 0.06		0.23 ± 0.02
total	1.34 ± 0.01	1.32 ± 0.01	1.20 ± 0.01	0.83 ± 0.02	0.70 ± 0.04

[a]HiF = high-frequency arc, MF = low-frequency arc. Please refer to Supplementary Figure S11 for the analysis of the impedance contributions.

conduction processes. This is also consistent with previous reports on mesoporous electrolytes.[9] As far as the mid frequency is concerned, the resulting C_{MF} is again compatible with a grain boundary conductivity effect, this time assuming a grain size ≈ 100 nm. This is in line with the overall particle size resulting from TEM investigations (cf. Figure 2). C_{MF} can therefore be tentatively assigned to electrical resistance at the contact between the different particles owing to the only partial sintering. The disappearance of such a contribution upon Co decoration is consistent with improved interparticle sintering. Please note that the sintering temperature employed here (800 °C) is high enough for activating the sintering process in Co-decorated ceria.[69]

Tailoring the Electrical Transport Character by Pr (Co-)Doping. The effect of Pr doping and (Pr, Gd) co-doping in the structural and electrochemical properties of mesoporous ceria has been assessed. Full TEM analysis was carried out on 10CGPO and CPO and is reported in Figure 6. HAADF-TEM imaging (Figure 6a,b for CPO and 10CGPO, respectively) confirms that the long-range mesoporous structure of the as-synthesized powders is present (cf. also Figures 2 and 3). To obtain local chemical information, we first carried out a qualitative elemental distribution inspection in the spectrum images by K-means clustering analysis (Figures 6c,d for CPO and 10CGPO, respectively) and an elemental quantification along EELS line-scans (Figure 6e,f) crossing grain boundary regions. In the case of CPO, a clear dopant segregation is observed both in the qualitative cluster analysis (Figure 6c lhs, regions 1 and 3) and in the quantification along the EELS line-scan (Figure 6e). The comparison of the latter with the as-synthesized CGO (cf. Figure 4e), however, suggests that, in CPO, a slightly lower tendency to dopant segregation is present (cf. dopant fraction maxima; [Pr]/[Ce] ∼0.6 vs [Gd]/[Ce] ∼0.8). This can be explained in light of the expected double valence for Pr (3+/4+). Particularly, for the Pr^{4+} fraction, both the electrostatic and elastic driving forces for dopant segregation are not present (the ionic radius of Pr^{4+} is comparable to that of Ce^{4+}).[70] In the case of CGPO, both dopants clearly tend to segregate toward the GBs and grain surfaces, as one can observe on the basis of the resolved cluster signals. The Pr/Ce and Gd/Ce white line ratios increase in regions 0 and 1 of panel d, as the Pr WLs (931−951 eV) and Gd WLs (1185−1217 eV) increase in intensity and the Ce WLs (883−901 eV) decrease. According to the elemental quantification along the line-scan (Figure 6e), an increment (up to 0.4) in the Gd/Ce and Pr/Ce molar ratios is observed, whereas these ratios remain close to the nominal values (0.11) at locations far from the GB. The Gd and Pr deviation profiles exhibit similar widths (∼1 nm) and concentration maxima.

Finally, in Figure 7, we report the results of the in-plane electrical measurements for films based on $Ce_{0.8}Gd_{0.2-x}Pr_xO_2$, x = 0, 0.05, 0.1, and 0.2 (values for CGO are reported again for the reader's convenience). In the Nyquist plots (650 °C, dry oxygen) reported in the inset of Figure 7a, one can observe two main contributions similar to the case of CGO. Fitting with a series of two ZARC elements (cf. also Supplementary Figure S9 for DRT analysis) results in a true capacitance C_{HiF} = 1−2·10^{-11} F/cm and C_{MF} in the order of 10^{-10}−10^{-9} F/cm for the high- and medium-frequency contribution, respectively. Interestingly, the total conductivity value is monotonically increasing for higher x ($0 \le x \le 0.1$). The activation energy for the total conductivity in CGPO ($0 \le x \le 0.1$) also presents a slight decrease upon Pr doping, as can be observed in Table 3. For x = 0.2 (CPO), the electrical behavior is remarkably different, as the slope of $\sigma_{tot,min}$ vs $1/T$ is much less pronounced and presents a kink at ≈600 °C indicating a change in the activation energy (from E_a = 0.83 eV for the low-T regime to E_a = 0.70 eV at high temperatures). The analysis of the single-impedance contributions, presented in Supplemen-

https://doi.org/10.1021/acs.jpcc.1c04861
J. Phys. Chem. C XXXX, XXX, XXX−XXX

tary Figure S11, shows that both impedance arcs are reduced by the addition of Pr.

The similar activation energies for all the CGPO samples analyzed, $0 \leq x \leq 0.1$ (cf. Table 2), indicate no change in the conduction mechanism; namely, in all cases, the material is mainly an ionic conductor. This is also confirmed by the sluggish pO_2 dependence of $\sigma_{tot,min}$, as reported in Supplementary Figure S12. The increase of total conductivity upon Pr introduction in CGO (co-doping) has been previously shown and mainly assigned to a decrease in the grain boundary resistance. Particularly, Luebke et al.[71] reported a ≈ 2-fold increase for CGPO pellets (□m-size grains), whereas Bowman et al.[50] observed up to 50 times increase in the grain boundary conductivity for $Gd_{0.11}Pr_{0.04}Ce_{0.85}O_2$ with respect to $Gd_{0.2}Ce_{0.8}O_2$. In our case, the net effect of (Pr, Gd) co-doping is a strong increase of the total conductivity of about 1 order of magnitude for 10CGPO compared to the as-synthesized CGO ($\sigma_{tot,min}$ = $2.2 \cdot 10^{-6}$ and $3.5 \cdot 10^{-7}$ $S \cdot cm^{-1}$ at 700 °C, respectively). We ascribe such a finding mainly to the segregation of Pr to the GBs (as highlighted in Figure 4), which is arguably expected to have a twofold effect: (i) Decrease of $[A'_{Ce}]$ at the GB (A acceptor dopant). By comparing Figures 4 and 6, one clearly observes a lower Gd concentration at the GB level in CGPO (maximum Gd/Ce cationic ratio ≈ 0.4) with respect to CGO (Gd/Ce ≈ 0.8; please note the different nominal Gd bulk concentration for the two). Although in CGPO a similar Pr accumulation is present locally at the GB (Pr/Ce ≈ 0.4), at least a fraction of such a dopant is expected to be oxidized (Pr^{4+}) under working conditions,[72] leading to a net decrease of 3+ charge at the GBs. This translates into a reduction of the oxygen vacancy migration energy due to reduced scattering. (ii) Occurrence of local electronic current through the grain boundaries stemming from the double Pr3+/4+ valence of Pr and leading to polaron hopping from Pr'_{Ce} to Pr^{x}_{Ce}.[72] Though the latter scenario is corroborated by a certain dependence especially of the MF contribution on pO_2 (cf. Supplementary Figure S12), no remarkable change in activation energy, which could possibly be associated to the appearance of a different conduction mechanism (cf. Table 3), was found. Please also note that previous Monte Carlo simulations predict increased bulk ionic conductivity for Gd−Pr co-doped ceria.[73]

Finally, in the case of CPO, as previously reported,[74] the material is a mixed ionic−electronic conductor in which the total conductivity is the sum of oxygen ion conductivity (σ_{Ion}) and the polaronic conductivity (σ_{Pr}) induced by the mixed valence of Pr: $\sigma_{tot} = \sigma_{Pr} + \sigma_{Ion}$. Notably, while σ_{Ion} is directly related to the polaron concentration (Pr ionization) via the electroneutrality equation ($2[V_O^{\cdot\cdot}] = [Pr'_{Ce}]$) and is therefore expected to increase in more reducing conditions (higher T or lower pO_2), polaron conductivity depends on the availability of neighboring hopping sites (Pr^{x}_{Ce}) and is a function of $[Pr^{x}_{Ce}] \times [Pr'_{Ce}]$.[74] This consideration allows explaining the observed T and pO_2 dependence for $\sigma_{tot,min}$ in CPO. The higher activation energy for T > 600 °C can be related to an increased ion transport number (increased ionic character of the electrical conductivity due to large $[Pr'_{Ce}]$) and reflects the higher migration enthalpy for oxygen vacancies with respect to polarons.[75] Similarly, also decreasing the pO_2 determines an enhancement of the ionic conductivity due to a decrease of $[Pr^{x}_{Ce}] \times [Pr'_{Ce}]$ (positive slope for $Log(G_{min})$ vs Log pO_2, Figure 7b).[75] Interestingly, a higher T corresponds to a weaker σ vs pO_2 relation and can again be related to a tendency toward Pr ionization.

CONCLUSIONS

In conclusion, we presented an in-depth structural and electrochemical analysis of hard-template nanocasted (Pr, Gd)-doped cerium oxide particles. 3D electron tomography allowed to obtain a detailed spatial reconstruction of the mesoporous particles, highlighting single and double gyroids with a narrow pore distribution (11 and 4 nm, respectively). A comparative assessment of the structural−functional relationship by means of complementary HR-TEM techniques, alongside impedance spectroscopy, pointed out that, while as-synthesized CGO exhibits a clear dopant segregation, this can be efficiently removed by mild HF post-treatment. This results in an improvement of 1 order of magnitude in the film ionic conductivity ($\sigma_{tot,min}$=$2.2 \cdot 10^{-6}$ $S \cdot cm^{-1}$ for HF-CGO at 720 °C) and is mainly ascribed to the removal of defect trapping effects at GBs. Co decoration of mesoporous powders induces, under the same conditions, an additional enhancement of the ionic conductivity ($\sigma_{tot,min}$=$2.8 \cdot 10^{-5}$ $S \cdot cm^{-1}$ at 720 °C) owing to better interparticle sintering. (Gd, Pr) co-doping is identified as an effective strategy to decrease the GB resistance (about 1 order of magnitude increase in the total conductivity for 10% Gd + 10% Pr with respect to mesoporous CGO), maintaining the ionic character of the material. Conversely, doping uniquely with Pr yields a mixed ionic−electronic conductor with reduced activation energy and increased ionicity for T > 600 °C. The present results offer a detailed fundamental analysis of nanocasted ceria and offer tools (surface and bulk chemical modifications) for tailoring its transport functionalities.

ASSOCIATED CONTENT

Supporting Information

The Supporting Information is available free of charge at https://pubs.acs.org/doi/10.1021/acs.jpcc.1c04861.

Morphological electron tomography for the CGPO mesoporous material; comparison between ADF experimental projections and projected images from the volume reconstructed; detailed process for the pore size distribution analysis from the projection images used in the ET reconstructions; grain structure characterization for the CGO, CGO-HF, and CGPO mesoporous materials via TEM and STEM experiments; DRT analysis for EIS spectra of CGO and CGPO samples; pO_2 dependence for the single-impedance contributions of CGO and CGPO films; and Arrhenius plots for the impedance contributions for films of CGPO and CGPO (PDF)

AUTHOR INFORMATION

Corresponding Authors

Federico Baiutti − *Catalonia Institute for Energy Research (IREC), Barcelona 08930, Spain;* orcid.org/0000-0001-9664-2486; Email: fbaiutti@irec.cat

Albert Tarancón − *Catalonia Institute for Energy Research (IREC), Barcelona 08930, Spain; ICREA, 23 Passeig Lluís Companys, Barcelona 08010, Spain;* orcid.org/0000-0002-1933-2406; Email: atarancon@irec.cat

https://doi.org/10.1021/acs.jpcc.1c04861
J. Phys. Chem. C XXXX, XXX, XXX−XXX

Authors

Javier Blanco-Portals − *LENS-MIND, Department of Electronics and Biomedical Engineering, Universitat de Barcelona, Barcelona 08028, Spain; Institute of Nanoscience and Nanotechnology (IN2UB), Universitat de Barcelona, Barcelona 08028, Spain;* orcid.org/0000-0002-7037-269X

Simone Anelli − *Catalonia Institute for Energy Research (IREC), Barcelona 08930, Spain*

au Torruella − *LENS-MIND, Department of Electronics and Biomedical Engineering, Universitat de Barcelona, Barcelona 08028, Spain; Institute of Nanoscience and Nanotechnology (IN2UB), Universitat de Barcelona, Barcelona 08028, Spain;* orcid.org/0000-0002-6864-4000

Miguel Lápez-Haro − *Departamento de Ciencia de los Materiales e Ingeniería Metalúrgica y Química Inorgánica, Facultad de Ciencias and Instituto Universitario de Investigación en Microscopía Electránica y Materiales (IMEYMAT), Facultad de Ciencias, Universidad de Cádiz, Campus Universitario de Puerto Real, Cádiz 11510, Spain;* orcid.org/0000-0003-2560-8015

José Calvino − *Departamento de Ciencia de los Materiales e Ingeniería Metalúrgica y Química Inorgánica, Facultad de Ciencias and Instituto Universitario de Investigación en Microscopía Electránica y Materiales (IMEYMAT), Facultad de Ciencias, Universidad de Cádiz, Campus Universitario de Puerto Real, Cádiz 11510, Spain;* orcid.org/0000-0002-0989-1335

Sonia Estradé − *LENS-MIND, Department of Electronics and Biomedical Engineering, Universitat de Barcelona, Barcelona 08028, Spain; Institute of Nanoscience and Nanotechnology (IN2UB), Universitat de Barcelona, Barcelona 08028, Spain*

Marc Torrell − *Catalonia Institute for Energy Research (IREC), Barcelona 08930, Spain*

Francesca Peirá − *LENS-MIND, Department of Electronics and Biomedical Engineering, Universitat de Barcelona, Barcelona 08028, Spain; Institute of Nanoscience and Nanotechnology (IN2UB), Universitat de Barcelona, Barcelona 08028, Spain*

Complete contact information is available at: https://pubs.acs.org/10.1021/acs.jpcc.1c04861

Author Contributions

$^{\nabla}$Equal contribution

Notes

The authors declare no competing financial interest.

■ ACKNOWLEDGMENTS

The authors acknowledge the financial support of the "Generalitat de Catalunya" (2017 SGR 1421, NANOEN) and MITECO for the financial support of the project 3DPASSION (PID2019-107106RB-C3119S01452-006). J.B.P., P.T., F.P., and S.E., from the Consolidated Research Group of the "Generalitat de Catalunya" MIND (Micro-nanotechnology and nanoscopies for electronic and photonic devices) (Ref. 2017 SGR 776), acknowledge the financial support from the Spanish Ministry of Science and Innovation (MICINN) through the project PID2019-106165GB-C21, the Spanish Research Network RED2018-102609-T, and the FI-AGAUR Research Fellowship Program, Generalitat de Catalunya (FI grant 2018FI_B_00360). They also acknowledge the use of instrumentation as well as the technical advice provided by the National Facility ELECMI ICTS, at DME-UCA and UMEAP-UB nodes, and the use of instrumentation in the NanoBioMedical Centre of the Adam Mickiewicz University in Poznan backed by the technical advice of Dr. Emerson Coy and Prof. Stefan Jurga. J.J.C. and M.L.H. acknowledge the financial support from FEDER/MICIIN (Proj. Ref. MAT2017-87579-R and PID2019-110018GA-I00). This work has also been co-financed by the 2014−2020 ERDF Operational Programme and by the Department of Economy, Knowledge, Business and University of the Regional Government of Andalusia. Project reference: FEDER-UCA18-107139.

■ REFERENCES

(1) Wan, Y.; Zhao. On the Controllable Soft-Templating Approach to Mesoporous Silicates. *Chem. Rev.* **2007**, *107*, 2821−2860.

(2) Deng, X.; Chen, K.; Tüysüz, H. Protocol for the Nanocasting Method: Preparation of Ordered Mesoporous Metal Oxides. *Chem. Mater.* **2017**, *29*, 40−52.

(3) Mamak, M.; Coombs, N.; Ozin, G. Self-Assembling Solid Oxide Fuel Cell Materials: Mesoporous Yttria-Zirconia and Metal-Yttria-Zirconia Solid Solutions. *J. Am. Chem. Soc.* **2000**, *122*, 8932−8939.

(4) Ramasamy, E.; Lee, J. Ordered Mesoporous SnO2-Based Photoanodes for High-Performance Dye-Sensitized Solar Cells. *J. Phys. Chem. C* **2010**, *114*, 22032−22037.

(5) Ramasamy, E.; Lee, J. Ferrocene-Derivatized Ordered Mesoporous Carbon as High Performance Counter Electrodes for Dye-Sensitized Solar Cells. *Carbon* **2010**, *48*, 3715−3720.

(6) Kang, E.; An, S.; Yoon, S.; Kim, J. K.; Lee, J. Ordered Mesoporous WO3-X Possessing Electronically Conductive Framework Comparable to Carbon Framework toward Long-Term Stable Cathode Supports for Fuel Cells. *J. Mater. Chem.* **2010**, *20*, 7416−7421.

(7) Wei, M.; Konishi, Y.; Zhou, H.; Yanagida, M.; Sugihara, H.; Arakawa, H. Highly Efficient Dye-Sensitized Solar Cells Composed of Mesoporous Titanium Dioxide. *J. Mater. Chem.* **2006**, *16*, 1287−1293.

(8) Jiao, F.; Shaju, K. M.; Bruce, P. G. Synthesis of Nanowire and Mesoporous Low-Temperature LiCoO2 by a Post-Templating Reaction. *Angew. Chem., Int. Ed. Engl.* **2005**, *117*, 6708−6711.

(9) Elm, M. T.; Hofmann, J. D.; Suchomski, C.; Janek, J.; Brezesinski, T. Ionic Conductivity of Mesostructured Yttria-Stabilized Zirconia Thin Films with Cubic Pore Symmetry—On the Influence of Water on the Surface Oxygen Ion Transport. *ACS Appl. Mater. Interfaces* **2015**, *7*, 11792−11801.

(10) Rolison, D. R. Catalytic Nanoarchitectures - The Importance of Nothing and the Unimportance of Periodicity. *Science* **2003**, *299*, 1698−1701.

(11) Zukalovà, M.; Zukal, A.; Kavan, L.; Nazeeruddin, M. K.; Liska, P.; Gràtzel, M. Organized Mesoporous TiO2 Films Exhibiting Greatly Enhanced Performance in Dye-Sensitized Solar Cells. *Nano Lett.* **2005**, *5*, 1789−1792.

(12) Almar, L.; Tarancán, A.; Andreu, T.; Torrell, M.; Hu, Y.; Dezanneau, G.; Morata, A. Mesoporous Ceramic Oxides as Humidity Sensors: A Case Study for Gadolinium-Doped Ceria. *Sens. Actuators, B* **2015**, *216*, 41−48.

(13) Zornoza, B.; Irusta, S.; Téllez, C.; Coronas, J. Mesoporous Silica Sphere-Polysulfone Mixed Matrix Membranes for Gas Separation. *Langmuir* **2009**, *25*, 5903−5909.

(14) Long, J. W.; Dunn, B.; Rolison, D. R.; White, H. S. Three-Dimensional Battery Architectures. *Chem. Rev.* **2004**, *104*, 4463−4492.

(15) Ye, Y.; Jo, C.; Jeong, I.; Lee, J. Functional Mesoporous Materials for Energy Applications: Solar Cells, Fuel Cells, and Batteries. *Nanoscale* **2013**, *5*, 4584−4605.

(16) Antonelli, D. M. Synthesis and Mechanistic Studies of Sulfated Meso- and Microporous Zirconias with Chelating Carboxylate Surfactants. *Adv. Mater.* **1999**, *11*, 487−492.

(17) Almar, L.; Andreu, T.; Morata, A.; Torrell, M.; Yedra, L.; Estradé, S.; Peirá, F.; Tarancán, A. High-Surface-Area Ordered

https://doi.org/10.1021/acs.jpcc.1c04861
J. Phys. Chem. C XXXX, XXX, XXX−XXX

Mesoporous Oxides for Continuous Operation in High Temperature Energy Applications. *J. Mater. Chem. A* **2014**, *2*, 3134−3141.
(18) Bork, A. H.; Carrillo, A. J.; Hood, Z. D.; Yildiz, B.; Rupp, J. L. M. Oxygen Exchange in Dual-Phase La0.65Sr0.35MnO3-CeO2Composites for Solar Thermochemical Fuel Production. *ACS Appl. Mater. Interfaces* **2020**, *12*, 32622−32632.
(19) Chueh, W. C.; Haile, S. M. A Thermochemical Study of Ceria: Exploiting an Old Material for New Modes of Energy Conversion and CO_2 Mitigation. *Philos. Trans. R. Soc., A* **2010**, *368*, 3269−3294.
(20) Mogensen, M.; Sammes, N. M.; Tompsett, G. A. Physical, Chemical and Electrochemical Properties of Pure and Doped Ceria. *Solid State Ionics* **2000**, *129*, 63−94.
(21) Almar, L.; Morata, A.; Torrell, M.; Gong, M.; Andreu, T.; Liu, M.; Tarancón, A. A Durable Electrode for Solid Oxide Cells: Mesoporous Ce0.8Sm0.2O1.9 Scaffolds Infiltrated with a Sm0.5Sr0.5CoO3-δ Catalyst. *Electrochim. Acta* **2017**, *235*, 646−653.
(22) Hernández, E.; Baiutti, F.; Morata, A.; Torrell, M.; Tarancón, A. Infiltrated Mesoporous Oxygen Electrodes for High Temperature Co-Electrolysis of H_2O and CO_2 in Solid Oxide Electrolysis Cells. *J. Mater. Chem. A* **2018**, *6*, 9699−9707.
(23) Anelli, S.; Baiutti, F.; Hornés, A.; Bernadet, L.; Torrell, M.; Tarancón, A. Improved Mesostructured Oxygen Electrodes for Highly Performing Solid Oxide Cells for Co-Electrolysis of Steam and Carbon Dioxide. *J. Mater. Chem. A* **2019**, *7*, 27458−27468.
(24) Anelli, S.; Hernández, E.; Bernadet, L.; Sun, X.; Hagen, A.; Baiutti, F.; Torrell, M.; Tarancón, A. Co-Electrolysis of Steam and Carbon Dioxide in Large Area Solid Oxide Cells Based on Infiltrated Mesoporous Oxygen Electrodes. *J. Power Sources* **2020**, *478*, 228774.
(25) Nicollet, C.; Kalaev, D.; Tuller, H. L. Mixed Conductivity and Oxygen Surface Exchange Kinetics of Lanthanum-Praseodymium Doped Cerium Dioxide. *Solid State Ionics* **2019**, *331*, 96−101.
(26) Zhang, T.; Hing, P.; Huang, H.; Kilner, J. Sintering and Grain Growth of CoO-Doped CeO 2 Ceramics. *J. Eur. Ceram. Soc.* **2002**, *22*, 27−34.
(27) De la Peña, F.; Prestat, E.; Fauske, V.T.; Burdet, P.; Jokubauskas, P.; Nord, M.; Ostasevicius, T.; MacArthur, K.E.; Sarahan, M.; Johnstone, D.N.; et al. *HyperSpy v1.5.2*; Zenodo, 2019.
(28) Pedregosa, F.; Varoquaux, G.; Gramfort, A.; Michel, V.; Thirion, B.; Grisel, O.; Blondel, M.; Prettenhofer, P.; Weiss, R.; Dubourg, V.; et al. Scikit-learn: Machine learning in Python. *J. Mach. Learn. Res.* **2011**, *12*, 2825−2830.
(29) Grisel, O.; Mueller, A.; Lars; Gramfort, A.; Louppe, G.; Prettenhofer, P.; Blondel, M.; Niculae, V.; Nothman, J.; Joly, A.; et al. *Scikit-Learn 0.24.1*; Zenodo, 2021.
(30) Torruella, P.; Estrader, M.; Lápez-Ortega, A.; Bará, M. D.; Varela, M.; Peirá, F.; Estradé, S. Clustering Analysis Strategies for Electron Energy Loss Spectroscopy (EELS). *Ultramicroscopy* **2018**, *185*, 42−48.
(31) Lápez-Haro, M.; Tinoco, M.; Fernández-Garcia, S.; Chen, X.; Hungria, A. B.; Cauqui, M. Á.; Calvino, J. J. A Macroscopically Relevant 3D-Metrology Approach for Nanocatalysis Research. *Part. Part. Syst. Charact.* **2018**, *35*, 1700343.
(32) Saghi, Z.; Divitini, G.; Winter, B.; Leary, R.; Spiecker, E.; Ducati, C.; Midgley, P. A. Compressed Sensing Electron Tomography of Needle-Shaped Biological Specimens − Potential for Improved Reconstruction Fidelity with Reduced Dose. *Ultramicroscopy* **2016**, *160*, 230−238.
(33) Thomas, J. M.; Leary, R.; Midgley, P. A.; Holland, D. J. A New Approach to the Investigation of Nanoparticles: Electron Tomography with Compressed Sensing. *J. Colloid Interface Sci.* **2013**, *392*, 7−14.
(34) Li, C. *Compressive Sensing for 3D Data Processing Tasks: Applications, Models and Algorithms*; Rice University, 2011.
(35) Li, C.; Yin, W.; Jiang, H.; Zhang, Y. An Efficient Augmented Lagrangian Method with Applications to Total Variation Minimization. *Comput. Optim. Appl.* **2013**, *56*, 507−530.
(36) Van Aarle, W.; Palenstijn, W. J.; De Beenhouwer, J.; Altantzis, T.; Bals, S.; Batenburg, K. J.; Sijbers, J. The ASTRA Toolbox: A Platform for Advanced Algorithm Development in Electron Tomography. *Ultramicroscopy* **2015**, *157*, 35−47.
(37) Judge, J. S. A Study of the Dissolution of SiO_2 in Acidic Fluoride Solutions. *J. Electrochem. Soc.* **1971**, *118*, 1772.
(38) Van der Heide, P. A. M.; Baan Hofman, M. J.; Ronde, H. J. Etching of Thin SiO_2 Layers Using Wet HF Gas. *J. Vac. Sci. Technol., A* **1989**, *7*, 1719−1723.
(39) Jud, E.; Huwiler, C. B.; Gauckler, L. J. Sintering Analysis of Undoped and Cobalt Oxide Doped Ceria Solid Solutions. *J. Am. Ceram. Soc.* **2005**, *88*, 3013−3019.
(40) Kim, D. J. Lattice Parameters, Ionic Conductivities, and Solubility Limits in Fluorite-Structure MO_2 Oxide [M = Hf^{4+}, Zr^{4+}, Ce^{4+}, Th^{4+}, U^{4+}] Solid Solutions. *J. Am. Ceram. Soc.* **1989**, *72*, 1415−1421.
(41) Tok, A. I. Y.; Du, S. W.; Boey, F. Y. C.; Chong, W. K. Hydrothermal Synthesis and Characterization of Rare Earth Doped Ceria Nanoparticles. *Mater. Sci. Eng., A* **2007**, *466*, 223−229.
(42) Zhao, D., Wan, Y.; Zhou, W., *Ordered Mesoporous Materials*; John Wiley & Sons, 2012
(43) Che, S.; Garcia-Bennett, A. E.; Liu, X.; Hodgkins, R. P.; Wright, P. A.; Zhao, D.; Terasaki, O.; Tatsumi, T.; Garcia-Bennett, A. E.; Terasaki, O.; et al. A. Synthesis of Large-Pore Ia3d Mesoporous Silica and Its Tubelike Carbon Replica. *Angew. Chem., Int. Ed.* **2003**, *42*, 3930−3934.
(44) Tian, B.; Liu, X.; Solovyov, L. A.; Liu, Z.; Yang, H.; Zhang, Z.; Xie, S.; Zhang, F.; Tu, B.; Yu, C.; Terasaki, O.; Zhao, D. Facile Synthesis and Characterization of Novel Mesoporous and Mesorelief Oxides with Gyroidal Structures. *J. Am. Chem. Soc.* **2004**, *126*, 865−875.
(45) Liante, L. A. *Ordered Mesoporous Metal Oxides for Solid Oxide Fuel Cells and Gas Sensors*; Ph.D. Dissertation, University of Barcelona: Spain, 2014.
(46) Shirpour, M.; Rahmati, B.; Sigle, W.; Van Aken, P. A.; Merkle, R.; Maier, J. Dopant Segregation and Space Charge Effects in Proton-Conducting $BaZrO_3$ Perovskites. *J. Phys. Chem. C* **2012**, *116*, 2453−2461.
(47) Bowman, W. J.; Kelly, M. N.; Rohrer, G. S.; Hernandez, C. A.; Crozier, P. A. Enhanced Ionic Conductivity in Electroceramics by Nanoscale Enrichment of Grain Boundaries with High Solute Concentration. *Nanoscale* **2017**, *9*, 17293−17302.
(48) Kim, D.; Bliem, R.; Hess, F.; Gallet, J. J.; Yildiz, B. Electrochemical Polarization Dependence of the Elastic and Electrostatic Driving Forces to Aliovalent Dopant Segregation on LaMnO3. *J. Am. Chem. Soc.* **2020**, *142*, 3548−3563.
(49) Lei, Y.; Ito, Y.; Browning, N. D.; Mazanec, T. J. Segregation Effects at Grain Boundaries in Fluorite-Structured Ceramics. *J. Am. Ceram. Soc.* **2002**, *85*, 2359−2363.
(50) Bowman, W. J.; Zhu, J.; Sharma, R.; Crozier, P. A. Electrical Conductivity and Grain Boundary Composition of Gd-Doped and Gd/Pr Co-Doped Ceria. *Solid State Ionics* **2015**, *272*, 9−17.
(51) Egerton, R. F. *Electron Energy-Loss Spectroscopy in the Electron Microscope*, Springer Science & Business Media , 2011, DOI: 10.1007/978-1-4419-9583-4.
(52) Hartmann, P.; Brezesinski, T.; Sann, J.; Lotnyk, A.; Eufinger, J. P.; Kienle, L.; Janek, J. Defect Chemistry of Oxide Nanomaterials with High Surface Area: Ordered Mesoporous Thin Films of the Oxygen Storage Catalyst CeO2-ZrO 2. *ACS Nano* **2013**, *7*, 2999−3013.
(53) Fleig, J. The Grain Boundary Impedance of Random Microstructures: Numerical Simulations and Implications for the Analysis of Experimental Data. *Solid State Ionics* **2002**, *150*, 181−193.
(54) Rupp, J. L. M.; Gauckler, L. J. Microstructures and Electrical Conductivity of Nanocrystalline Ceria-Based Thin Films. *Solid State Ionics* **2006**, *177*, 2513−2518.
(55) Bae, J.; Lim, Y.; Park, J.-S.; Lee, D.; Hong, S.; An, J.; Kim, Y.-B. Thermally-Induced Dopant Segregation Effects on the Space Charge Layer and Ionic Conductivity of Nanocrystalline Gadolinia-Doped Ceria. *J. Electrochem. Soc.* **2016**, *163*, F919−F926.

(56) Pérez-Coll, D.; Sánchez-Lápez, E.; Mather, G. C. Influence of Porosity on the Bulk and Grain-Boundary Electrical Properties of Gd-Doped Ceria. *Solid State Ionics* **2010**, *181*, 1033−1042.
(57) Göbel, M. C.; Gregori, G.; Guo, X.; Maier, J. Boundary Effects on the Electrical Conductivity of Pure and Doped Cerium Oxide Thin Films. *Phys. Chem. Chem. Phys.* **2010**, *12*, 14351−14361.
(58) Celik, E.; Ma, Y.; Brezesinski, T.; Elm, M. T. Ordered Mesoporous Metal Oxides for Electrochemical Applications: Correlation between Structure, Electrical Properties and Device Performance. *Phys. Chem. Chem. Phys.* **2021**, *23*, 10706−10735.
(59) Guo, X.; Sigle, W.; Maier, J. Blocking Grain Boundaries in Yttria-Doped and Undoped Ceria Ceramics of High Purity. *J. Am. Ceram. Soc.* **2003**, *86*, 77−87.
(60) Ge, L.; Ni, Q.; Cai, G.; Sang, T.; Guo, L. Improving SiO_2 Impurity Tolerance of $Ce_{0.8}Sm_{0.2}O_{1.9}$: Synergy of CaO and ZnO in Scavenging Grain-Boundary Resistive Phases. *J. Power Sources* **2016**, *324*, 582−588.
(61) Ding, Y.; Choi, Y. M.; Chen, Y.; Pradel, K. C.; Liu, M.; Wang, Z. L. Quantitative Nanoscale Tracking of Oxygen Vacancy Diffusion inside Single Ceria Grains by in Situ Transmission Electron Microscopy. *Mater. Today* **2020**, *38*, 24−34.
(62) Kim, S.; Maier, J. On the Conductivity Mechanism of Nanocrystalline Ceria. *J. Electrochem. Soc.* **2002**, *149*, J73.
(63) Tschöpe, A.; Kilassonia, S.; Birringer, R. The Grain Boundary Effect in Heavily Doped Cerium Oxide. *Solid State Ionics* **2004**, *173*, 57−61.
(64) Kim, S. Isn't the Space-Charge Potential in Ceria-Based Solid Electrolytes Largely Overestimated. *Phys. Chem. Chem. Phys.* **2016**, *18*, 19787−19791.
(65) Souza, E. C. C.; Chueh, W. C.; Jung, W.; Muccillo, E. N. S.; Haile, S. M. Ionic and Electronic Conductivity of Nanostructured, Samaria-Doped Ceria. *J. Electrochem. Soc.* **2012**, *159*, 127−135.
(66) Zhou, X.-D.; Huebner, W.; Kosacki, I.; Anderson, H. U. Microstructure and Grain-Boundary Effect on Electrical Properties of Gadolinium-Doped Ceria. *J. Am. Ceram. Soc.* **2002**, *85*, 1757−1762.
(67) Avila-Paredes, H. J.; Kim, S. The Effect of Segregated Transition Metal Ions on the Grain Boundary Resistivity of Gadolinium Doped Ceria: Alteration of the Space Charge Potential. *Solid State Ionics* **2006**, *177*, 3075−3080.
(68) Lewis, G. S.; Atkinson, A.; Steele, B. C. H.; Drennan, J. Effect of Co Addition on the Lattice Parameter, Electrical Conductivity and Sintering of Gadolinia-Doped Ceria. *Solid State Ionics* **2002**, *152-153*, 567−573.
(69) Jud, E.; Gauckler, L. J. Sintering Behavior of Cobalt Oxide Doped Ceria Powders of Different Particle Sizes. *J. Electroceram.* **2005**, *14*, 247−253.
(70) Shannon, R. D. Revised Effective Ionic Radii and Systematic Studies of Interatomic Distances in Halides and Chalcogenides. *Acta Crystallogr. Sect. A* **1976**, *32*, 751−767.
(71) Lübke, S.; Wiemhöfer, H.-D. Electronic Conductivity of Gd-Doped Ceria with Additional Pr-Doping. *Solid State Ionics* **1999**, *117*, 229−243.
(72) Bishop, S. R.; Stefanik, T. S.; Tuller, H. L. Electrical Conductivity and Defect Equilibria of $Pr_{0.1}Ce_{0.9}O_{2-\delta}$. *Phys. Chem. Chem. Phys.* **2011**, *13*, 10165−10173.
(73) Dholabhai, P. P.; Adams, J. B.; Crozier, P. A.; Sharma, R. In Search of Enhanced Electrolyte Materials: A Case Study of Doubly Doped Ceria. *J. Mater. Chem.* **2011**, *21*, 18991−18997.
(74) Lenser, C.; Gunkel, F.; Sohn, Y. J.; Menzler, N. H. Impact of Defect Chemistry on Cathode Performance: A Case Study of Pr-Doped Ceria. *Solid State Ionics* **2018**, *314*, 204−211.
(75) Tuller, H. L.; Bishop, S. R.; Chen, D.; Kuru, Y.; Kim, J. J.; Stefanik, T. S. Praseodymium Doped Ceria: Model Mixed Ionic Electronic Conductor with Coupled Electrical, Optical, Mechanical and Chemical Properties. *Solid State Ionics* **2012**, *225*, 194−197.

https://doi.org/10.1021/acs.jpcc.1c04861
J. Phys. Chem. C XXXX, XXX, XXX−XXX